Hard-X-ray dark-field imaging using a grating interferometer

F. PFEIFFER[1,2]*, M. BECH[3], O. BUNK[1], P. KRAFT[1], E. F. EIKENBERRY[1], CH. BRÖNNIMANN[1], C. GRÜNZWEIG[1] AND C. DAVID[1]

[1]Paul Scherrer Institut, CH-5232 Villigen PSI, Switzerland
[2]École Polytechnique Fédérale de Lausanne, CH-1015 Lausanne, Switzerland
[3]Niels Bohr Institute, University of Copenhagen, DK-2100 Copenhagen, Denmark
*e-mail: franz.pfeiffer@psi.ch

Published online: 13 January 2008; doi:10.1038/nmat2096

Imaging with visible light today uses numerous contrast mechanisms, including bright- and dark-field contrast, phase-contrast schemes and confocal and fluorescence-based methods[1]. X-ray imaging, on the other hand, has only recently seen the development of an analogous variety of contrast modalities. Although X-ray phase-contrast imaging could successfully be implemented at a relatively early stage with several techniques[2–11], dark-field imaging, or more generally scattering-based imaging, with hard X-rays and good signal-to-noise ratio, in practice still remains a challenging task even at highly brilliant synchrotron sources[12–18]. In this letter, we report a new approach on the basis of a grating interferometer that can efficiently yield dark-field scatter images of high quality, even with conventional X-ray tube sources. Because the image contrast is formed through the mechanism of small-angle scattering, it provides complementary and otherwise inaccessible structural information about the specimen at the micrometre and submicrometre length scale. Our approach is fully compatible with conventional transmission radiography and a recently developed hard-X-ray phase-contrast imaging scheme[11]. Applications to X-ray medical imaging, industrial non-destructive testing and security screening are discussed.

Visible-light microscopy is a standard and widely used tool with a broad range of applications in science, industry and everyday life. Besides standard bright-field imaging, many more contrast mechanisms have been developed, and dark-field-imaging, phase-contrast, confocal and fluorescence microscopy are routine methods in today's light-microscopy applications[1]. It is not surprising that this development has stimulated a similar progress in imaging applications with other forms of radiation. In electron microscopy, for example, where the first electron-microscope image was produced in the early 1930s, dark-field imaging was introduced in the late 1930s[19], and imaging on the basis of phase contrast in the 1940s[20].

In X-ray microscopy, or more generally X-ray imaging, the development of a similar range of contrast modalities proceeded much more slowly and is still a very active field of research. Despite the early pioneering work on X-ray interferometry in the 1960s[2], the majority of phase-contrast imaging[2–11] and dark-field imaging[12–18] methods were introduced in the late 1990s. The development of such advanced imaging methods is particularly difficult for hard X-rays (with energies in the multi-keV range), because of the lack of efficient X-ray optics. Existing hard-X-ray dark-field-imaging methods, for example, rely on the use of crystal optics that can accept only a very narrow energy bandwidth (≈0.01%) and angular divergence[3,15–18] (≈1 arcsec). This is why dark-field or scattering-based imaging is currently restricted in practice to applications at highly brilliant synchrotron X-ray sources[14–18] and is not available for widespread applications that require a method applicable to standard X-ray tubes. In the following we describe a new approach, which helps overcome these restrictions and can produce high-quality X-ray dark-field scatter images using conventional X-ray tube sources.

Figure 1 shows our experimental arrangement. It consists of a source grating G0, a phase grating G1 and an analyser absorption grating G2 (Fig. 1a). The source grating (G0), typically placed close to the X-ray tube, is an aperture mask with transmitting slits. It creates an array of periodically repeating line sources and effectively enables the use of relatively large, that is, square-millimetre-sized, X-ray sources, without compromising the coherence requirements of the arrangement formed by G1 and G2 (ref. 11). The image contrast itself is formed via the combined effect of the two gratings G1 and G2. The second grating (G1) acts as a phase mask, and imprints periodic phase modulations onto the incoming wave field. Through the Talbot effect[21–24], the phase modulation is transformed into an intensity modulation in the plane of G2, forming a linear periodic fringe pattern perpendicular to the optical axis and parallel to the lines of G1 (Fig. 1b). The third grating (G2), with absorbing lines and the same periodicity and orientation as the fringes created by G1, is placed in the detection plane, immediately in front of the detector. When one of the gratings is scanned along the transverse direction x_g, the intensity signal $I(m,n)$ in each pixel (m,n) in the detector plane oscillates as a function of x_g (Fig. 1c).

The fundamental idea of the method presented here is to evaluate the local changes of the oscillation $I(m,n,x_g)$ induced by an object and determine from these several imaging signals, including the dark-field contrast. To analyse these changes quantitatively, we write the intensity oscillation for each detector pixel in a Fourier series

$$I(m,n,x_g) = \sum_i a_i(m,n)\cos(ikx_g + \phi_i(m,n)) \approx a_0(m,n) + a_1(m,n)\cos(kx_g + \phi_1(m,n)), \quad (1)$$

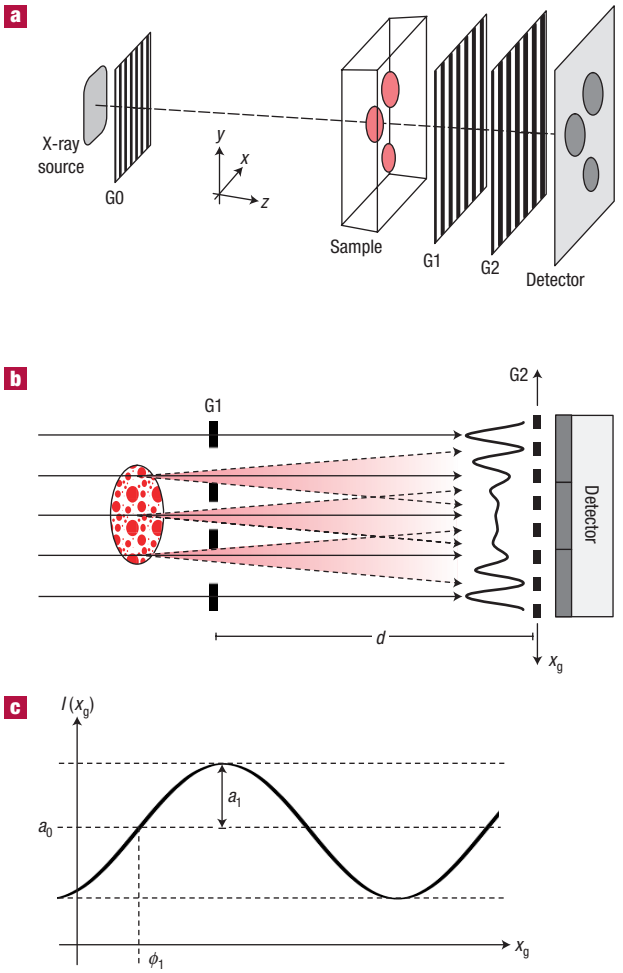

Figure 1 X-ray grating interferometer. a, Set-up with a source grating G0, a phase grating G1 and an analyser absorption grating G2. **b**, Through the Talbot effect a linear periodic fringe pattern is created behind G1 in the plane of G2. **c**, Intensity modulation detected in a detector pixel when one of the gratings is scanned along x_g. A loss in the amplitude of the oscillation due to the scattering of X-rays in the specimen (degradation of the coherent wavefront) can be used to extract images with dark-field contrast.

where a_i are the amplitude coefficients, ϕ_i the corresponding phase coefficients, $k = 2\pi/p_2$ and p_2 is the period of G2. Then the normalized average transmission of the specimen in each detector pixel is given by $T(m,n) = a_0^s(m,n)/a_0^r(m,n)$, where the superscripts s and r denote the values measured with the specimen in place (^{s}) and as a reference without (^{r}). Note that $T(m,n)$ is identical to what would be measured with a conventional X-ray radiography set-up. Furthermore, we have previously shown[11] that differential phase-contrast images can be obtained by analysing the lateral shift of intensity modulation, that is, the quantity $\phi_1(m,n)$ in equation (1).

The new aspect and particular focus of the work presented here is how dark-field images, or more generally images on the basis of the local scattering power of the sample, can be obtained with such a set-up. In terms of visible-light Fourier optics, dark-field illumination removes the zeroth order (unscattered light) from the diffraction pattern formed at the rear focal plane of the objective. This results in an image formed exclusively from higher-angle diffraction intensities scattered by the specimen. Quite similarly, information about the scattering power of the specimen is contained in our case in the higher order, that is, the first Fourier component of $I(m,n,x_g)$. More precisely, the amplitude of the first Fourier component, a_1, is decreased when X-rays are scattered or reflected at internal inhomogeneities or interfaces on their passage through the specimen (Fig. 1b).

For a quantitative description of this effect, we first define the normalized oscillation amplitude, the visibility of the intensity modulation of $I(m,n,x_g)$, by the ratio $V^r(m,n) \equiv (I_{max} - I_{min})/(I_{max} + I_{min}) = a_1^r(m,n)/a_0^r(m,n)$; see equation (1). The relative decrease of the visibility due to the specimen can be quantified by defining the normalized visibility, $V(m,n) \equiv V^s(m,n)/V^r(m,n)$. For homogeneous specimens, that is, for samples with negligible small-angle X-ray scattering contribution, the value for the visibility remains unchanged, and $V(m,n) = 1$. However, specimens that, for example, show strong internal density fluctuations on micrometre length scales, and thus produce a strong small-angle X-ray scattering signal, show a significant decrease of the visibility and yield values of $V < 1$ (ref. 23). More generally, we note that the quantity $V(m,n)$ is inversely proportional to the effective integrated local small- (and ultrasmall-) angle scattering power of the sample and therefore refer to it as a 'dark-field' image of the specimen. Most simply, this can be understood by considering that the amplitude of the oscillations in $I(m,n,x_g)$ is most effectively reduced by X-rays scattered from the object at wavevectors corresponding to diffraction angles defined by the ratio of half the period of G2 over the distance between the object and G2 (see also Fig. 1b).

Figure 2 shows the experimental results obtained for a test sample made out of a Teflon plastic tube and a natural rubber tube. The conventional transmission image is shown in Fig. 2a, the novel dark-field image in Fig. 2b and the differential phase-contrast image in Fig. 2c (ref. 11). Whereas the inner part of the two tubes looks very similar in the transmission image (Fig. 2a) and the differential phase-contrast image (Fig. 2c), clear differences are visible in the dark-field image (Fig. 2b). The microscopic density fluctuations (pore structure) in the rubber tube produce a strong small-angle scattering signal and thus significantly smaller intensity modulations (Fig. 2d) in $I(m,n,x_g)$ and correspondingly low values in the dark-field image (Fig. 2b). The inner parts of the Teflon tube, on the other hand, show no significant contributions to the dark-field signal, because the plastic is a homogenous material with essentially no density fluctuations on the relevant length scales. However, at the interfaces of the Teflon tube, small-angle reflections reveal more structural details. Both the dark-field image (Fig. 2b) and the differential phase-contrast image show (Fig. 2c), more clearly than the absorption image (Fig. 2a), that the thick walls of the Teflon tube were actually made by inserting a thinner tube into a tube with a larger diameter.

More generally, the small-angle scattering signal as recorded in the dark-field image is particularly sensitive to density variations in the object on the length scale of a few tenths of nanometres to several micrometres. It naturally complements the length scales that can be imaged directly by radiographic methods into the submicrometre range.

Although we have applied our method to obtain dark-field images of numerous specimens, proving the method to be of potential interest for a broad range of applications, we can report here on only one in detail (a second is in the Supplementary Information, Fig. S2). This example is shown in Fig. 3 and particularly demonstrates the potential for improved contrast in medical imaging. As a biological test specimen, a chicken wing was used. The conventional transmission contrast is shown in Fig. 3a and the dark-field contrast in Fig. 3b. Note that, because both

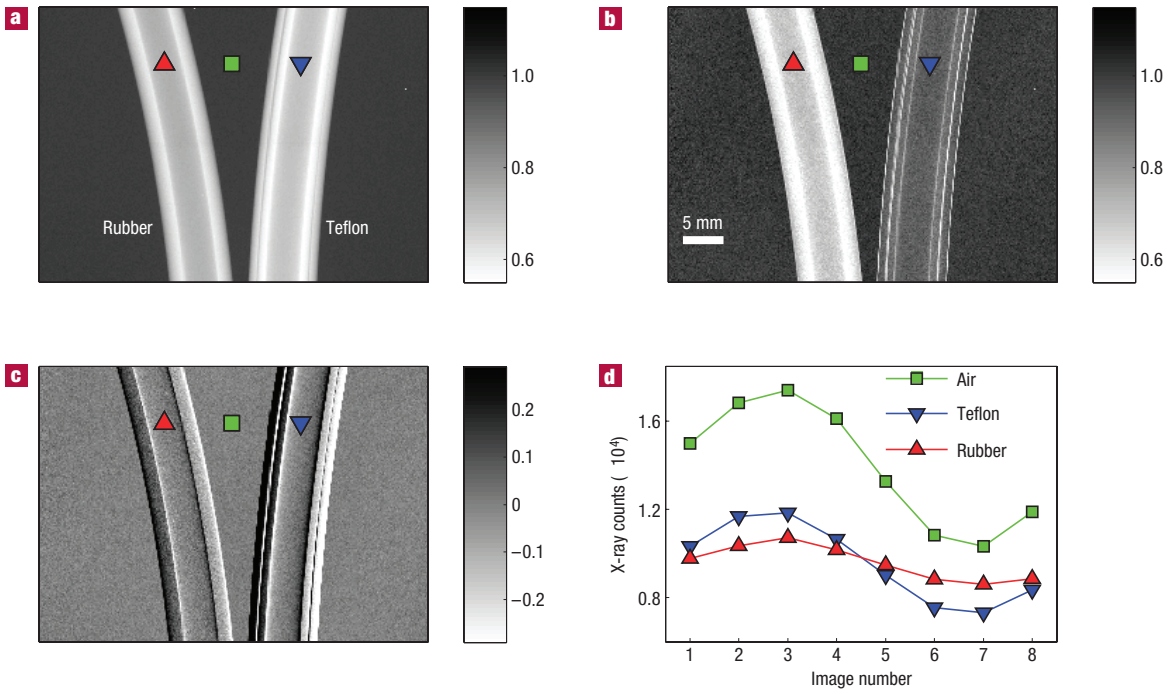

Figure 2 X-ray imaging of a test sample consisting of a PTFE (Teflon) plastic tube and a natural rubber tube. a, Conventional X-ray transmission image (normalized to the empty beam). **b**, Dark-field image of the same sample (normalized visibility, see text). **c**, Differential phase-contrast image. All images are shown on a linear grey scale. **d**, Intensity oscillations for three detector pixels extracted from a series of eight images taken at different values of x_g. Clearly visible is the loss of fringe visibility in the detector pixel behind the natural rubber tube due to the strong small-angle scattering produced by microscopic density fluctuations (pore structure). The total exposure time for the whole data set was 40 s.

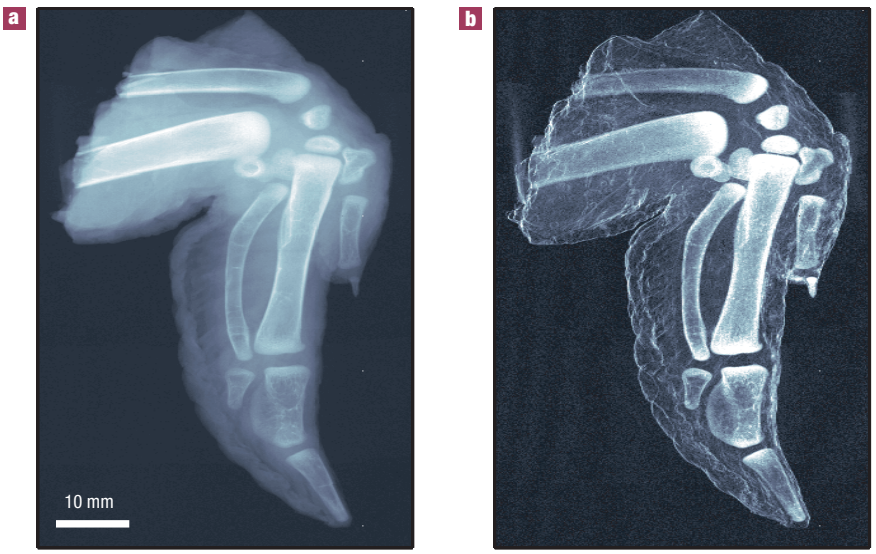

Figure 3 Imaging of a biological specimen (chicken wing). a, Conventional transmission image. **b**, Dark-field image. The X-ray scattering due to the porous microstructure of the bones and the reflection at internal or external interfaces produce a strong signal in the dark-field image. The total exposure time to obtain the whole data set, from which the images were processed, was 40 s. Both images are shown on a linear grey scale corresponding to four times the standard deviation of the range of pixel grey-scale values.

images were obtained from the same data set, the radiation dose was identical in both cases.

In agreement with what was observed in the images of the tube sample (Fig. 2), we find that also in this biological specimen the boundaries and interfaces produce a strong signal in the dark-field image (see Fig. 3b). Furthermore, we observe that the chicken bones obviously consist of a highly porous and strongly scattering microstructure, because they are clearly visible in the dark-field

contrast (Fig. 3b). However, it is surprising that the differences in the grey-scale values of the bone and the tissue are significantly different in Fig. 3a and b. Although the soft tissue provides a still well-defined signal in the transmission image, the scattering of the tissue is obviously too weak to produce a significant contribution to the dark-field image contrast. We conclude that, although bones are generally already well represented in the transmission images, dark-field imaging can potentially yield a complementary and even enhanced contrast[17,18]. For example, in cases of complicated bone fractures, where small splinters can intrude into the surrounding tissue, dark-field contrast could provide the necessary specificity to visualize subtle details.

In summary, we have shown how a grating interferometer can be used to produce dark-field images with hard X-rays. We have demonstrated that, in contrast to existing crystal-analyser-based methods[15–18], our method can efficiently be implemented with a standard X-ray tube source. The approach is potentially interesting for a wide range of applications including medical imaging[18], security screening[25] (see Supplementary Information, Fig. S2), industrial non-destructive testing[26], food inspection and small-animal imaging. In future, a further increase in the sensitivity of the method could also provide contrast between healthy and diseased breast tissue, because breast tumours show a different small-angle scattering signature than the healthy adipose matrix[27,28]. Generally, we believe that the method is of particular interest for challenging X-ray imaging applications, because it simultaneously provides dark-field, transmission and differential phase contrast, thus providing maximum information about the specimen (see Supplementary Information, Fig. S1). Finally, this approach can be extended into three dimensions using computer tomographic techniques, coupled with a synchrotron source to yield micrometre-resolution hard-X-ray dark-field images, or implemented with other types of radiation, such as neutrons.

METHODS

The experiments were carried out on a Seifert ID 3000 X-ray generator operated at 40 kV/30 mA. We used a tungsten (W) line focus tube (DX-W8 × 0.4-L) with a focus size of 8 (horizontal) ×0.4 (vertical) mm^2. Owing to the inclination of the target with respect to the optical axis of 6°, the effective source size was 0.8 (h) × 0.4 (v) mm^2.

The gratings were fabricated by a process involving photolithography, deep etching into silicon and electroplating of gold[29]. The size of the active area was limited in the present study by the processing technology (100 mm wafers) to 64 × 64 mm^2. No principle constraints hinder the upscaling of the method to larger areas. The gratings had periods of $p_0 = 73\,\mu m$, $p_1 = 3.9\,\mu m$ and $p_2 = 2.0\,\mu m$. The heights of the grating structures, which were optimized for a mean X-ray energy of 28 keV, were 42 μm (G0), 35 μm (G1) and 26 μm (G2). The distance between G0 and G1 was 1.57 m and that between G1 and G2 43 mm, corresponding to the first fractional Talbot distance[24].

The images were recorded using a PILATUS 100K pixel detector[30]. The module consists of an array of 487 × 195 pixels, with a pixel size of 0.172 × 0.172 mm^2. For the results shown in Fig. 3, three images were stacked on top of one another to increase the field of view in the vertical direction. The quantum detection efficiency is determined by the probability of absorbing an X-ray in the 320-μm-thick Si sensor and is ≃10% (at 28 keV). For the results shown in Figs 2 and 3, a series of eight individual images with exposure times of 5 s each was recorded. We believe that the exposure time can be reduced by at least by a factor of 60 by (1) using a rotating-anode X-ray generator with a power of a ≥10 kW, instead of the current 1 kW (a factor of 10), (2) increasing the detector efficiency from currently 10% to 30% using a thicker sensor (a factor of three) and (3) decreasing the distance between the source and the sample (a factor of two).

The two polytetrafluoroethylene (PTFE, Teflon) plastic tubes used in the experiment had a density of $\rho_{PTFE} = 2.2\,g\,cm^{-3}$ and a radius of $R_1 = 4.0\,mm$ with a hollow core of $r_1 = 3.0\,mm$ and $R_2 = 3.0\,mm$ with $r_2 = 2.0\,mm$, respectively. The natural rubber tube had a density of $\rho_{rubber} \approx 1.13\,g\,cm^{-3}$ and a radius of $R = 4.0\,mm$ with a hollow core of $r = 2.0\,mm$.

To extract the dark-field, phase and absorption contrast signals from the measured intensity modulation $I(m, n, x_g)$, one-dimensional discrete fast Fourier transforms were computed for each pixel. The resulting values for the Fourier coefficients were normalized to the corresponding values obtained without the specimen in place. On a standard personal computer (1.7 GHz processor, 2 GByte memory), the processing time needed for a series of eight images with 10^5 pixels was of the order of a few seconds.

Received 18 September 2007; accepted 26 November 2007; published 13 January 2008.

References

1. Murphy, D. B. *Fundamentals of Light Microscopy and Electronic Imaging* (Wiley, New York, 2001).
2. Bonse, U. & Hart, M. An X-ray interferometer with long separated interfering beam paths. *Appl. Phys. Lett.* **6**, 155–156 (1965).
3. Davis, T. J., Gao, D., Gureyev, T. E., Stevenson, A. W. & Wilkins, A. W. Phase-contrast imaging of weakly absorbing materials using hard X-rays. *Nature* **373**, 595–598 (1995).
4. Ingal, V. N. & Beliaevskaya, E. A. X-ray plane-wave topography observation of the phase contrast from non-crystalline objects. *J. Phys. D* **28**, 2314–2317 (1995).
5. Chapman, D. *et al.* Diffraction enhanced x-ray imaging. *Phys. Med. Biol.* **42**, 2015–2025 (1997).
6. Snigirev, A., Snigireva, I., Kohn, V., Kuznetsov, S. & Schelokov, I. On the possibilities of X-ray phase contrast microimaging by coherent high-energy synchrotron radiation. *Rev. Sci. Instrum.* **66**, 5486–5492 (1995).
7. Wilkins, S. W., Gureyev, T. E., Gao, D., Pogany, A. & Stevenson, A. W. Phase-contrast imaging using polychromatic hard X-rays. *Nature* **384**, 335–337 (1996).
8. Momose, A. Recent advances in X-ray phase imaging. *Japan J. Appl. Phys.* **44**, 6355–6267 (2005).
9. Momose, A., Yashiro, W., Takeda, Y., Suzuki, Y. & Hattori, T. Phase tomography by X-ray Talbot interferometry for biological imaging. *Japan J. Appl. Phys.* **45**, 5254–5262 (2006).
10. Weitkamp, T. *et al.* Quantitative X-ray phase imaging with a grating interferometer. *Opt. Express* **13**, 6296–6304 (2005).
11. Pfeiffer, F., Weitkamp, T., Bunk, O. & David, C. Phase retrieval and differential phase-contrast imaging with low-brilliance X-ray sources. *Nature Phys.* **2**, 258–261 (2006).
12. Morrison, G. R. & Browne, M. T. Dark-field imaging with the scanning-transmission X-ray microscope. *Rev. Sci. Instrum.* **63**, 611–614 (1992).
13. Chapman, H. N., Jacobsen, C. & Williams, S. A characterisation of dark-field imaging of colloidal gold labels in a scanning transmission X-ray microscope. *Ultramicroscopy* **62**, 191–213 (1996).
14. Suzuki, Y. & Uchida, F. Dark-field imaging in hard X-ray scanning microscopy. *Rev. Sci. Instrum.* **66**, 1468–1470 (1995).
15. Pagot, E. *et al.* A method to extract quantitative information in analyzer-based X-ray phase contrast imaging. *Appl. Phys. Lett.* **82**, 3421–3423 (2003).
16. Levine, L. E. & Long, G. G. X-ray imaging with ultra-small-angle X-ray scattering as a contrast mechanism. *J. Appl. Cryst.* **37**, 757–765 (2004).
17. Ando, M. *et al.* Clinical step onward with X-ray dark-field imaging and perspective view of medical applications of synchrotron radiation in Japan. *Nucl. Instrum. Methods A* **548**, 1–16 (2005).
18. Shimao, D., Sugiyama, H., Kunisada, T. & Ando, M. Articular cartilage depicted at optimized angular position of Laue angular analyzer by X-ray dark-field imaging. *Appl. Radiat. Isot.* **64**, 868–874 (2006).
19. von Ardenne, M. Das Elektronen-Rastermikroskop. *Z. Tech. Phys.* **19**, 407–416; *Z. Phys.* **109**, 553–572 (1938).
20. Ramberg, E. G. Phase contrast in electron microscope images. *J. Appl. Phys.* **20**, 441–444 (1949).
21. Lohmann, A. W. & Silva, D. E. An interferometer based on the Talbot effect. *Opt. Commun.* **2**, 413–415 (1971).
22. Yokozeki, S. & Suzuki, T. Shearing interferometer using grating as beam splitter. *Appl. Opt.* **10**, 1575–1579 (1971).
23. Pfeiffer, F. *et al.* Shearing interferometer for quantifying the coherence of hard X-ray beams. *Phys. Rev. Lett.* **94**, 164801 (2005).
24. Weitkamp, T., David, C., Kottler, C., Bunk, O. & Pfeiffer, F. Tomography with grating interferometers at low-brilliance sources. *SPIE Int. Soc. Opt. Eng.* **6318**, 28–32 (2006).
25. Harding, G. X-ray scatter tomography for explosives detection. *Radiat. Phys. Chem.* **71**, 869–881 (2004).
26. Harding, G. & Schreiber, B Coherent X-ray scatter imaging and its applications in biomedical science and industry. *Radiat. Phys. Chem.* **56**, 229–245 (1999).
27. Fernandez, M. *et al.* Small-angle X-ray scattering studies of human breast tissue samples. *Phys. Med. Biol.* **47**, 577–592 (2002).
28. Fernandez, M. *et al.* Human breast cancer in vitro: Matching histo-pathology with small-angle X-ray scattering and diffraction enhanced X-ray imaging. *Phys. Med. Biol.* **50**, 2991–3006 (2005).
29. David, C. *et al.* Fabrication of diffraction gratings for hard X-ray phase contrast imaging. *Microelectron. Eng.* **84**, 1172–1177 (2007).
30. Bech, M. *et al.* X-Ray imaging with the PILATUS 100K detector. *Appl. Radiat. Isot.* (2007, in the press) (doi:10.1016/j.apradiso.2007.10.003).

Acknowledgements

We gratefully acknowledge C. Kottler for help with the experiments and T. Weitkamp and S. Wilkins for discussions.
Correspondence and requests for materials should be addressed to F.P.
Supplementary Information accompanies this paper on www.nature.com/naturematerials.

Author contributions

F.P., M.B. and C.D. conceived the experimental set up. C.D. and C.G. designed and fabricated the gratings. O.B. interfaced the experimental hardware and data acquisition system. F.P. wrote the data analysis software. C.B., E.F.E. and P.K. were responsible for the detector hardware, software and calibration. F.P. and M.B. analysed and interpreted the data.